

SANDIA REPORT

SAND2013-7713

Unlimited Release

Printed 17 September 2013

Athermalized Channeled Spectropolarimeter Enhancement

Julia Craven Jones, Brandyn M. Way, Jeff Hunt, Jeffrey A. Mercier

Prepared by
Sandia National Laboratories
Albuquerque, New Mexico 87185 and Livermore, California 94550

Sandia National Laboratories is a multi-program laboratory managed and operated by Sandia Corporation, a wholly owned subsidiary of Lockheed Martin Corporation, for the U.S. Department of Energy's National Nuclear Security Administration under contract DE-AC04-94AL85000.

Approved for public release; further dissemination unlimited.



Sandia National Laboratories

Issued by Sandia National Laboratories, operated for the United States Department of Energy by Sandia Corporation.

NOTICE: This report was prepared as an account of work sponsored by an agency of the United States Government. Neither the United States Government, nor any agency thereof, nor any of their employees, nor any of their contractors, subcontractors, or their employees, make any warranty, express or implied, or assume any legal liability or responsibility for the accuracy, completeness, or usefulness of any information, apparatus, product, or process disclosed, or represent that its use would not infringe privately owned rights. Reference herein to any specific commercial product, process, or service by trade name, trademark, manufacturer, or otherwise, does not necessarily constitute or imply its endorsement, recommendation, or favoring by the United States Government, any agency thereof, or any of their contractors or subcontractors. The views and opinions expressed herein do not necessarily state or reflect those of the United States Government, any agency thereof, or any of their contractors.

Printed in the United States of America. This report has been reproduced directly from the best available copy.

Available to DOE and DOE contractors from

U.S. Department of Energy
Office of Scientific and Technical Information
P.O. Box 62
Oak Ridge, TN 37831

Telephone: (865) 576-8401
Facsimile: (865) 576-5728
E-Mail: reports@adonis.osti.gov
Online ordering: <http://www.osti.gov/bridge>

Available to the public from

U.S. Department of Commerce
National Technical Information Service
5285 Port Royal Rd.
Springfield, VA 22161

Telephone: (800) 553-6847
Facsimile: (703) 605-6900
E-Mail: orders@ntis.fedworld.gov
Online order: <http://www.ntis.gov/help/ordermethods.asp?loc=7-4-0#online>



Athermalized Channeled Spectropolarimeter Enhancement

Julia Craven Jones, Brandyn M. Way, Jeffrey A. Mercier
Mission Science and Analysis
Jeff Hunt,
Optical Payload Design and Realization
Sandia National Laboratories
P.O. Box 5800
Albuquerque, New Mexico 87185-MS0406

Abstract

Channeled spectropolarimetry can measure the complete polarization state of light as a function of wavelength. Typically, a channeled spectropolarimeter uses high order retarders made of uniaxial crystal to amplitude modulate the measured spectrum with the spectrally-dependent Stokes polarization information. A primary limitation of conventional channeled spectropolarimeters is related to the thermal variability of the retarders. Thermal variation often forces frequent system recalibration, particularly for field deployed systems. However, implementing thermally stable retarders, made of biaxial crystal, results in an athermal channeled spectropolarimeter that relieves the need for frequent recalibration. This report presents experimental results for an athermalized channeled spectropolarimeter prototype produced using potassium titanyl phosphate. The results of this prototype are compared to the current thermal stabilization state of the art. Finally, the application of the technique to the thermal infrared is studied, and the athermalization concept is applied to an infrared imaging spectropolarimeter design.

ACKNOWLEDGEMENTS

This work was funded by the Early Career LDRD program.

CONTENTS

Contents	5
1. Introduction.....	9
1.1. Introduction to Channeled Spectropolarimetry.....	9
1.2 Thermal Instability.....	12
1.3 Producing a Thermally Stable Retarder.....	13
2. Athermalized Channeled Spectropolarimeter Prototype	15
2.1 Thermally Stable Retarder Design.....	15
2.2 Experimental Prototype Setup and Results.....	18
2.2 Tolerance Assessment.....	20
3. Comparison to a Multi-Material Approach.....	23
4. Application to the Thermal Infrared	25
5. Snapshot Imaging Spectropolarimeter Design.....	29
6. Conclusions.....	34
7. References.....	36
Distribution	38

FIGURES

Figure 1. Schematic of a CSP system. To incorporate a complete polarization measurement, two retarders, R_1 and R_2 , and an analyzer A are placed in series before a dispersive of interferometric (FTS) spectrometer.	10
Figure 2. An example of an interferogram obtained from a modulated output spectrum. The channels in the interferogram are labeled C_i , where $i = 0,1,2,3$ contain the polarimetric information.....	11
Figure 3. Example of thermally induced reconstruction errors in Stokes parameters S_1 , S_2 , and S_3 , across the VISNIR produced in (a) a conventional CSP system using quartz, and (b) a KTP ACSP system. A 5 °C change in temperature between calibration and data acquisition was used.	13
Figure 4. A biaxial crystal used at a TI-orientation, with the position of the three indices of refraction shown. In this figure, $n_1 = n_x$, $n_2 = n_y$, and $n_3 = n_z$. Light incident at the TI-angle will experience all three indices.....	16
Figure 5. (a) Dispersion of KTP simulated using Sellmeier equations from Error! Reference source not found.. (b) TI-Angle for KTP in the visible and NIR spectrum as a function of wavelength.....	17
Figure 6. Schematic of the refractive index orientation within a TI-oriented KTP phase retarder.	18
Figure 7. ACSP design and testing. (a) Experimental setup for proof of concept testing of a partial ACSP using the BTI-cut KTP retarder. (b) The BTI retarder is produced using the TI-angle identified by Ebberts [8].....	18

Figure 8. Simulated (a) and experimental (b) ACSP modulated spectral data for ambient, +11 °C and +21 °C above ambient. The consistency in the carrier frequency is indicative of the thermal stability of the retarder. Example reconstructions from the ACSP prototype are depicted in (c). 19

Figure 9. Error in the S_1 Stokes parameter as a function of AOI and temperature in an athermalized KTP phase retarder of $100\mu\text{m OPD}$. The region enclosed by the white lines represents where the error will not exceed more than 3% error of the expected value at $0.6328\mu\text{m}$ 21

Figure 10. Comparison of RPC for the two TI retarder approaches. The experimentally measured KTP BTI RPC and the anticipated RPC, based on tabulated thermo-optic coefficients, for the KTP BTI approach are depicted along with the anticipated RPC for the multi-material approach. 23

Figure 11. Transmission of RTA as a function of wavelength, in nm. 25

Figure 12. (a) AOI and Temperature tolerance per $100\mu\text{m OPD}$ for an RTA TI-phase retarder. The area enclosed by the white lines represents regions which are expected to exhibit S_1 Stokes parameter reconstruction percent error of less than 3% at $\lambda = 4\mu\text{m}$. (b) TI-angle as a function of wavelength over the visible and mid-wave infrared which deviates by less than 1.04° over $3\text{-}5\mu\text{m}$ from the value at $4\mu\text{m}$ 26

Figure 13. Transmission of LIGe and other similar materials. LGTe has a larger transmission range but this material does not have an orthorhombic crystalline structure. 27

Figure 14. (a) TI-angle as a function of wavelength in LIGe which deviates by less than 0.02° over $8\text{-}12\mu\text{m}$. (b) AOI and Temperature tolerance per $100\mu\text{m OPD}$ for a LIGe TI-phase retarder. The region enclosed by the white lines represents where S_1 reconstruction will exhibit a percent error of less than 3% at $10\mu\text{m}$ 27

Figure 15. Zemax layout of the SCAMPI prototype. The system is designed to operate in the SWIR. Combining an ACSP with an image slicing spectrometer, the system operates as a snapshot imaging spectropolarimeter. 30

Figure 16. The SCAMPI image slicer spectrometer incorporates a 5 by 7 lenslet array that produces 35 sub-images, each containing the dispersed and CSP-modulated spectra for a one dimensional slice of the composite image. 30

Figure 17. Residual phase change (RPC) for the KTP BTI retarder design for SCAMPI. The RPC as a function of field angle and change of temperature is depicted in (a) for $\lambda=1.3\mu\text{m}$. The maximum RPC as a function of wavelength over the sensor passband is depicted in (b). 32

Figure 18. Deviations in the reconstructed Stokes parameters for the Stokes parameter values producing (a) the maximum reconstruction error and (b) the minimum reconstruction error. 33

Figure 19. Fringe profiles for (a) the on-axis field point and (b) the $(2.5^\circ, 0^\circ)$ field point for the SCAMPI design using a KTP BTI retarder. 33

TABLES

Table 1. RMS error in ACSP reconstructions using ambient versus high temperature reference data. 20

Table 2. Optical properties of the MWIR candidate crystals. 25

Table 3. Optical properties of LWIR candidate crystals. 27

NOMENCLATURE

ACSP	Athermal Channeled Spectropolarimeter
BTI	Biaxial Thermally Insensitive
CSP	Channeled Spectropolarimetry
DOE	Department of Energy
FOV	Field of View
FFOV	Full Field of View
KTP	Potassium Titanyl Phosphate
SNL	Sandia National Laboratories
TI	Thermally Insensitive

1. INTRODUCTION

Channeled spectropolarimetry (CSP) is a no-moving-parts spectropolarimetric measurement technique that can be used with either dispersive or interferometric (Fourier transform) spectrometers [1, 2]. Developed extensively over the past decade, CSP instruments have been demonstrated in the visible and infrared for laboratory-based characterization of materials, remote sensing, and polarimetric imaging (see [3-6] for examples).

Interest in using channeled spectropolarimeters for field-based remote sensing measurements has produced a demand for CSP sensors that can be deployed without the need for frequent system recalibration. This report presents a technique for modifying a channeled spectropolarimeter sensor to provide for improved thermal stability. Section 1 provides an introduction to the CSP technique. This is followed by a discussion of the athermalized CSP design and results from a laboratory prototype in section 2. The results of the prototype are compared to the current thermal stabilization state of the art in section 3. Section 4 presents the design options for implementing the athermalized CSP in the thermal infrared. Finally, section five presents an initial design for a SWIR snapshot imaging thermally stable channeled spectropolarimeter.

1.1. Introduction to Channeled Spectropolarimetry

Polarimetric information, namely information indicative of the polarization state of incident light, can be exploited to characterize surface features or material properties [7]. The state of polarization of light can be quantified by the use of Stokes parameters. Stokes parameters are typically provided in the form which displays all four parameters as a Stokes vector. The definition of each parameter is given by

$$S = \begin{pmatrix} S_0 \\ S_1 \\ S_2 \\ S_3 \end{pmatrix} = \begin{pmatrix} I_H + I_V \\ I_H - I_V \\ I_{45} - I_{135} \\ I_R - I_L \end{pmatrix}. \quad (1)$$

In Eq. 1, the S_i are the Stokes parameters and the intensity term $I_H/I_V/I_{45}/I_{135}$ represents the intensity measured behind a linear analyzer with its transmission axis oriented along the horizontal/vertical/45°/135°. S_0 corresponds to the polarization independent intensity, while S_1 represents the preference for horizontal linear over vertical linear polarization. The third parameter, S_2 , represents the preference for linear +45° over linear 135°, and the fourth parameter, S_3 , represents the preference of the light for right hand circular over left hand circular polarization. The measurement of all four parameters fully characterizes the polarization state of incident light, and each Stokes parameter in Eq. 1 is implicitly dependent on wavenumber, $\sigma = 1/\lambda$.

Typically, a CSP system incorporates two high order uniaxial crystal retarders and an analyzer with a spectrometer, as depicted in Figure 1. The two retarders, R_1 and R_2 , have fast axis orientations of 0° (horizontal, or along the y-axis) and 45°, respectively, while the analyzer is parallel to R_1 at 0°. This configuration modulates the measured spectrum with carrier frequencies, the amplitudes of which contain the spectrally-dependent Stokes parameters $S_0(\sigma)$, $S_1(\sigma)$, $S_2(\sigma)$, and $S_3(\sigma)$. The intensity measured by the spectrometer will follow

$$I(\sigma) = \frac{1}{2} [S_0(\sigma) + S_1(\sigma) \cos(\phi_2) + S_2(\sigma) \sin(\phi_1) \sin(\phi_2) + S_3(\sigma) \cos(\phi_1) \sin(\phi_2)]. \quad (2)$$

In Eq. 2, $\phi_i(\sigma) = 2\pi\sigma B l_i$ is the phase difference introduced by the i^{th} retarder, $B = n_e - n_o$ is the birefringence of the crystal, l_i is the retarder thickness, and $\sigma = 1/\lambda$. Thus, with minimal additional complexity, a CSP system provides a complete Stokes polarization measurement that is acquired simultaneously with the spectrometer's spectral measurement. Note that a CSP can be produced using either a dispersive or an interferometric (Fourier transform) spectrometer. For the work discussed in this paper, a dispersive spectrometer based approach is implemented.

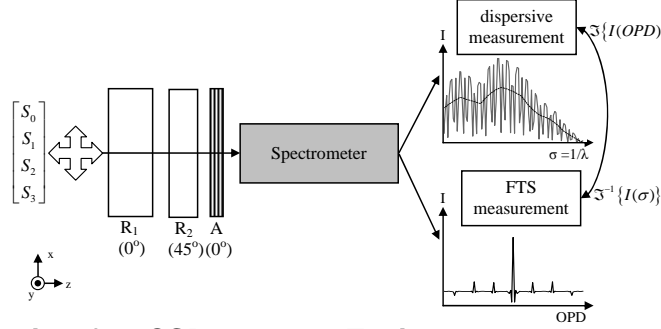


Figure 1. Schematic of a CSP system. To incorporate a complete polarization measurement, two retarders, R_1 and R_2 , and an analyzer A are placed in series before a dispersive or interferometric (FTS) spectrometer.

The configuration of the retarders and the polarizer in the CSP produces a phase delay that each Stokes parameter experiences differently. For example, light with an initial horizontal polarization ($S_1/S_0 = 1$) will propagate through R_1 unaltered but will experience a phase delay due to the orientation of R_2 . Conversely, incident light on the CSP which is oriented at a 45° degree angle with respect to the horizontal ($S_2/S_0 = 1$) will experience a phase delay by passing through R_1 and subsequently experience another phase delay by passing through R_2 . The phase delay produced by the combination of the two retarders varies linearly with wavenumber and will result in spectrally varying polarization orientations exiting R_2 . The analyzer acts as a filter which modulates the measured spectrum with the carrier frequencies induced by the phase retarders.

Determining the Stokes parameters from the modulated output spectrum involves exploiting a Fourier transform algorithm and a polarimetric calibration technique to characterize the phase terms induced by the retarders. First, the modulated output spectrum (collected with a dispersive CSP) must be sampled uniformly in wavenumber. A Fourier transform then converts the intensity spectrum into an interferogram. This is analogous to the interferogram obtained using an interferometric CSP. An example of the interferogram obtained using a CSP is shown in Figure 2 for 1:2 retarder thickness ratio ($d_1:d_2$). In this figure, the channels which contain the polarization information are labeled.

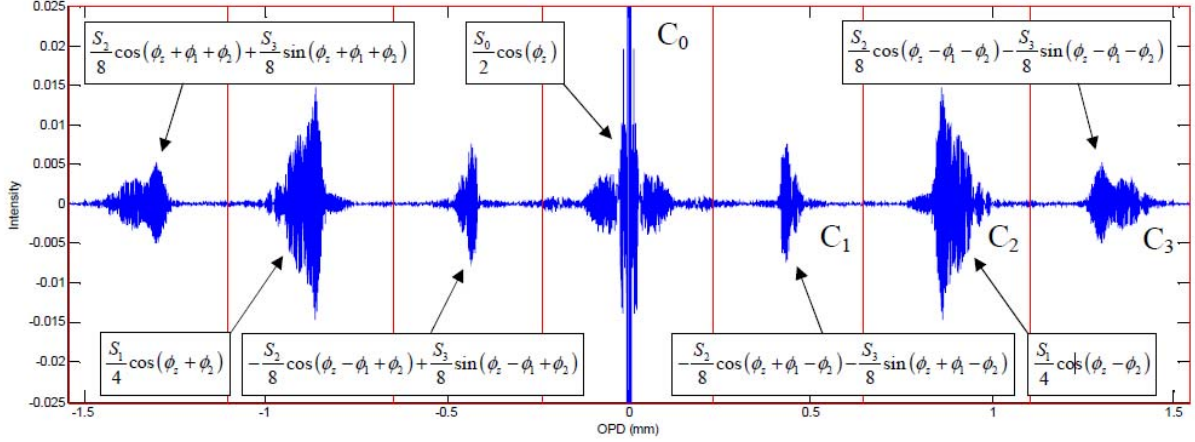


Figure 2. An example of an interferogram obtained from a modulated output spectrum. The channels in the interferogram are labeled C_i , where $i = 0,1,2,3$ contain the polarimetric information.

Although seven channels are produced in the interferogram, only three channels must be isolated (using Hamming filters) to extract the Stokes parameters. Using channels C_0 , C_1 , and C_2 , as labeled in Figure 2, provides

$$\mathfrak{T}(C_0) = \frac{1}{2} S_0(\sigma), \quad (3)$$

$$\mathfrak{T}(C_1) = \frac{1}{8} (S_2(\sigma) - jS_3(\sigma)) \exp(-j\phi_1) \exp(-j\phi_2), \quad (4)$$

and

$$\mathfrak{T}(C_2) = \frac{1}{4} S_1(\sigma) \exp(-j\phi_2). \quad (5)$$

In Eqs. 3-5, $\mathfrak{T}(C_i)$ represents the Fourier transform of the i^{th} channel.

However, the Stokes parameters S_1 , S_2 , and S_3 are still subject to the carrier frequency modulations induced by the CSP. The demodulation is obtained through a polarimetric calibration technique. The technique used in the report is known as the reference beam calibration technique [8], although another method does exist [8]. The reference beam calibration technique accounts for the phase modulations by using a known reference measurement. Specifically, light with a known polarization state is propagated through the CSP and the previously described Fourier algorithm is applied to the resulting modulated spectrum. This data is subsequently used as a reference. The phase information can then be removed from an unknown sample measurement using

$$S_{0,reference}(\sigma) = \left| \mathfrak{T}(C_{0,reference}) \right|, \quad (6)$$

$$S_{0,sample}(\sigma) = \left| \mathfrak{T}(C_{0,sample}) \right|, \quad (7)$$

$$S_{1,sample}(\sigma) = \frac{1}{\sqrt{2}} \operatorname{Re} \left| \frac{\mathfrak{I}(C_{2,sample}) \mathfrak{I}(C_{0,reference})}{\mathfrak{I}(C_{2,reference}) \mathfrak{I}(C_{0,sample})} \right|, \quad (8)$$

$$S_{2,sample}(\sigma) = \frac{1}{\sqrt{2}} \operatorname{Re} \left| \frac{\mathfrak{I}(C_{3,sample}) \mathfrak{I}(C_{0,reference})}{\mathfrak{I}(C_{3,reference}) \mathfrak{I}(C_{0,sample})} \right|, \quad (9)$$

and

$$S_{3,sample}(\sigma) = \frac{1}{\sqrt{2}} \operatorname{Im} \left| \frac{\mathfrak{I}(C_{3,sample}) \mathfrak{I}(C_{0,reference})}{\mathfrak{I}(C_{3,reference}) \mathfrak{I}(C_{0,sample})} \right|. \quad (10)$$

In Eqs. 6-10, the ‘reference’ and ‘sample’ subscripts are used to denote the known and unknown state of polarization measurements, respectively. Additionally, Eqs. 6-10 assume that the reference polarization state is fully linearly polarized at 22.5° ($S_1/S_0=S_2/S_0=0.707$).

1.2 Thermal Instability

The primary complication related to this reference beam calibration technique arises when sample data is acquired at a different temperature than the reference. Temperature produces a variation in thickness and dispersion of the birefringent retarder elements, changing in the carrier frequencies in the modulated spectral measurements. The change in phase of the i^{th} retarder for a change of temperature ΔT is given by

$$\Delta\phi_i \approx 2\pi\sigma l_i \Delta T \left[B(\sigma)\gamma_L + \left(\frac{\partial n_e}{\partial T} - \frac{\partial n_o}{\partial T} \right) \right], \quad (11)$$

where $\gamma_L = (1/l_i)(\partial l_i / \partial T)$ is the coefficient of linear thermal expansion along the propagation direction.

Eq. 11 implies that when the calibration data is applied after the instrument experiences a change in temperature, the carrier frequency phases are not effectively removed. This produces calibration errors in the polarization data products. As an example, a visible-near infrared (VNIR) CSP system was simulated assuming 32.5 and 10.8 mm thick quartz retarders that introduce approximately 300 and 100 μm of optical path difference (OPD) for R_1 and R_2 , respectively. The simulation used a spectrally invariant incident Stokes vector of $S_{in}/S_0 = [S_0 \ S_1 \ S_2 \ S_3]^T = [1; 0.8; -0.5; 0.3]$. Figure 3 (a) depicts the calibration error induced by a 5°C change in temperature of the quartz retarders between the acquisition of the reference and sample data. The reconstructed and known Stokes values are plotted to illustrate the significant deviation of the reconstructed values versus the true input polarization state.

As this example suggests, to avoid thermal errors in reconstructed data products, calibration data must be taken frequently, or precise thermal stability of the system must be maintained actively. Both of these solutions complicate field deployment significantly. An alternative self-calibration technique has been developed in attempts to circumvent these thermal errors [8]. However, this calibration method does not provide for direct measurement of all CSP retarder phase values, leading to uncertainty in the calibration. Instead, if a thermally insensitive (TI) retarder can be

produced, the reference beam calibration technique can be used without the need for frequent recalibration.

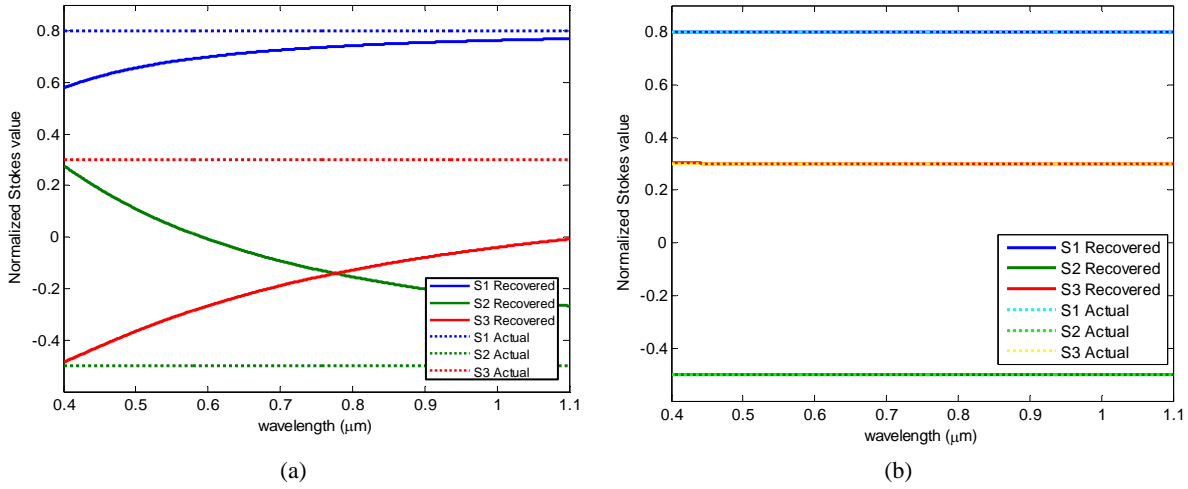


Figure 3. Example of thermally induced reconstruction errors in Stokes parameters S_1 , S_2 , and S_3 , across the VISNIR produced in (a) a conventional CSP system using quartz, and (b) a KTP ACSP system. A 5 °C change in temperature between calibration and data acquisition was used.

1.3 Producing a Thermally Stable Retarder

A TI retarder can be produced by taking advantage of the three distinct indices of refraction in a biaxial crystal. Previous work by others produced a biaxial thermally insensitive (BTI) crystal for an unrelated application using potassium titanyl phosphate (KTP) [9]. By modifying the BTI design presented in [9] to produce a high order TI retarder for channeled spectropolarimetry, an athermal channeled spectropolarimeter (ACSP) can be produced. To simulate the polarimetric reconstruction errors that can be anticipated with a KTP-based ACSP setup, the simulation scenario presented in Figure 3 (a) was repeated with BTI KTP retarders instead of quartz. Figure 3 (b) depicts the reconstructed Stokes parameters for a 5° C temperature change using the ACSP system. Comparing to the results in Figure 3 (a), the reconstructed Stokes parameters demonstrate a significantly enhanced correspondence to the input polarization state.

Alternatively, the use of multiple crystal materials has also been proposed and demonstrated as an approach to producing such a TI retarder [10]. A comparison of the BTI thermal stabilization results to the multi-material approach will be discussed in section 3.

2. ATHERMALIZED CHanneLED SPECTROPOLARIMETER PROTOTYPE

Using the BTI concept discussion in section 1, a thermally stable retarder suitable for CSP implementation is designed and demonstrated using a laboratory CSP prototype. The results of this effort are reviewed in this section.

2.1 Thermally Stable Retarder Design

The phase delay of a retarder, ϕ , can be expressed as a function of wavelength (λ), birefringence ($n_e - n_o$), and retarder thickness (L), and is given by

$$\phi = \frac{2\pi}{\lambda} (n_e - n_o) L. \quad (12)$$

For conventional uniaxial retarders, the birefringence and the thickness of the element are both functions of temperature. The total phase delay produced by a phase retarder after experiencing a change in temperature ΔT can be approximately described by

$$\phi_{total} \approx \phi + \frac{\delta\phi}{\delta T} \Delta T, \quad (13)$$

where $\frac{\partial\phi}{\partial T}$ is given by

$$\frac{\partial\phi}{\partial T} = \frac{2\pi L}{\lambda} \left[\frac{\partial n_e}{\partial T} - \frac{\partial n_o}{\partial T} + \alpha_{uniaxial} (n_e - n_o) \right]. \quad (14)$$

In Eq. 14, the term $\frac{\partial\phi}{\partial T}$ represents the change in phase difference with respect to temperature, the terms $\frac{\partial n_e}{\partial T}$ and $\frac{\partial n_o}{\partial T}$ represent the thermo-optic dispersion coefficients, and $\alpha_{uniaxial}$ represents the coefficient of thermal expansion. By combining terms, $\frac{\partial\phi}{\partial T}$ can be considered a function of effective thermal indices n'_e and n'_o , such that

$$\frac{\partial\phi}{\partial T} = \frac{2\pi L}{\lambda} (n'_e - n'_o), \quad (15)$$

where

$$n'_e = \frac{\partial n_e}{\partial T} + \alpha_{uniaxial} n_e, \quad (16)$$

and

$$n'_o = \frac{\partial n_o}{\partial T} + \alpha_{uniaxial} n_o. \quad (17)$$

The TI-orientation for a phase retarder is defined as the orientation such that the left side of Eq. 15 vanishes [9]. For a uniaxial crystal, the only orientation that meets this stipulation is such that

the light propagates along the extraordinary axis, n_e' . Although this orientation provides thermal stability, it does not serve well as a phase retarder because the two indices of refraction observed by incident radiation are equal.

An alternative solution involves using a biaxial crystal which has three unequal indices of refraction. The indices of refraction must satisfy the following relationship: $n_x' < n_y' < n_z'$. These indices represent the X, Y, and Z axes of the crystal. Using this notation, Eq. 14 can be revised to represent a biaxial crystal and is given by

$$\frac{\partial \phi_{BTI}}{\partial T} = \frac{2\pi L}{\lambda} \left[\frac{\partial n_y}{\partial T} - \frac{\partial n_{XZ}}{\partial T} + \alpha_{biaxial} (n_y - n_{XZ}) \right]. \quad (18)$$

Here $\frac{\partial \phi_{BTI}}{\partial T}$ is the thermal phase change experienced by the BTI crystal. The variables $\frac{\partial n_{XZ}}{\partial T}$, n_{XZ} , and $\alpha_{biaxial}$ represent parameters which are formed by a combination of two indices of the biaxial crystal and are given by

$$n_{XZ} = \frac{n_x n_z}{\left[n_z^2 \cos^2(\theta) + n_x^2 \sin^2(\theta) \right]^{1/2}}, \quad (19)$$

$$\alpha_{biaxial} = \left[\alpha_z \cos^2(\theta) + \alpha_x \sin^2(\theta) \right], \text{ and} \quad (20)$$

$$\frac{\partial n_{XZ}}{\partial T} = \frac{n_{XZ}^3}{n_x^3} \frac{\partial n_x}{\partial T} \cos^2(\theta) + \frac{n_{XZ}^3}{n_z^3} \frac{\partial n_z}{\partial T} \sin^2(\theta). \quad (21)$$

In Eqs. 19 - 21, θ represents the direction propagated by the incident radiation defined from the Z axis, as depicted in Figure 4. Figure 4 also illustrates how incident radiation on a phase retarder can experience a combination of two indices of refraction.

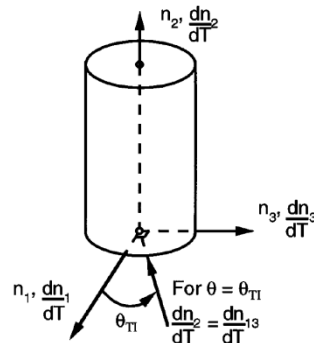


Figure 4. A biaxial crystal used at a TI-orientation, with the position of the three indices of refraction shown. In this figure, $n_1 = n_x$, $n_2 = n_y$, and $n_3 = n_z$. Light incident at the TI-angle will experience all three indices.

A biaxial crystal can produce $\frac{\partial \phi_{BTI}}{\partial T} = 0$ if the change in refractive index due to temperature in one axis is cancelled by the change in another, or

$$\frac{\delta n_{XZ}}{\delta T} + \alpha_{biaxial} n_{XZ} = \frac{\delta n_Y}{\delta T} + \alpha_{biaxial} n_Y. \quad (22)$$

By setting the left side of Eq. 18 equal to zero, the expression can be solved for θ_{TI} using both Eqs. 19 - 21, and the approximation that $(n_{XZ} / n_X)^3 \approx (n_{XZ} / n_Z)^3 \approx 1$ [9]. The resulting expression for θ_{TI} is given by

$$\theta_{TI} = \arccos \left(\frac{n'_Z - n'_Y}{n'_Z - n'_X} \right)^{1/2}. \quad (23)$$

For the purposes of creating a proof-of-concept device that could demonstrate the viability of an athermal channeled spectropolarimeter (ACSP), a biaxial crystal that meets the requirements stipulated in the previous section needed to be identified. The material Potassium Titanyl Phosphate (KTiOPO₄), better known as KTP, was selected. KTP is a commonly used material for frequency doubling and it is readily available from numerous vendors. The material was selected for our purposes because of its biaxial structure, birefringence, transparency in the visible spectrum, wide availability, and demonstrated TI properties [9]. Figure 5 (a) depicts the dispersion of KTP simulated using Sellmeier coefficients from [11]. Previous work provided a theoretical TI value of $\theta_{TI} = 32.0^\circ$ at $\lambda = 0.6328 \mu m$ and an experimentally verified value of $\theta_{TI} = 33.7^\circ$ at $\lambda = 0.6328 \mu m$ [9]. The experimental value was used to design the KTP phase retarder for the ACSP prototype with a $\pm 0.5^\circ$ manufacture tolerance. Figure 6 depicts the TI-oriented KTP phase retarder fabricated for the ACSP prototype.

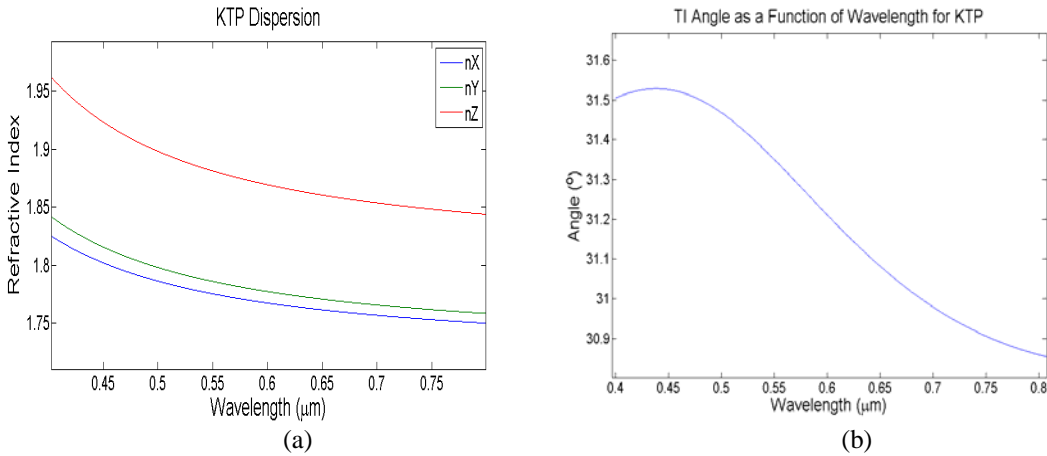


Figure 5. (a) Dispersion of KTP simulated using Sellmeier equations from Error! Reference source not found.. (b) TI-Angle for KTP in the visible and NIR spectrum as a function of wavelength.

Using the thermal properties of KTP [12] and dispersion information [11], the TI-angle in KTP was simulated over the visible and NIR and is depicted in Figure 5 (b). The simulated value for

θ_{TI} at $\lambda = 0.6328\mu\text{m}$ yielded a value of 31.17° , which deviates by 2.3% from the simulated value reported previously [9]. The reason for this deviation is most likely due to discrepancies in the dispersion data for KTP from one reference to another. Over the spectral region shown in Figure 5 (b), there is a variation of 0.7° in the TI-angle.

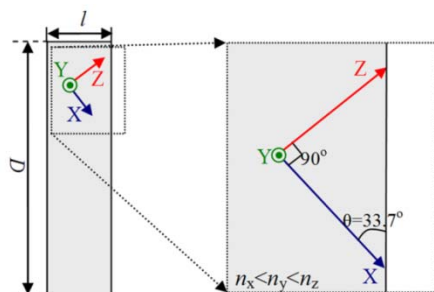


Figure 6. Schematic of the refractive index orientation within a TI-oriented KTP phase retarder.

2.2 Experimental Prototype Setup and Results

Proof of concept experiments in the visible spectral region were performed to provide experimental verification of the ACSP concept [13]. A diagram of the measurement methodology is depicted in Figure 7 (a). A quartz tungsten halogen (QTH) lamp serves a collimated white light source. A generating polarizer (G) creates a known and stable input polarization state. The BTI retarder (R) is made of KTP and has a nominal thickness of $l = 4.75$ mm, and is cut to the athermal prescription described in [9], as depicted in Figure 7 (b). The BTI retarder is aligned with its y-axis (as labeled in Figure 7 (b)) at 45° relative to the horizontal and is mechanically mounted to a hotplate. This is followed by an analyzing polarizer (A) to unify the polarization state.

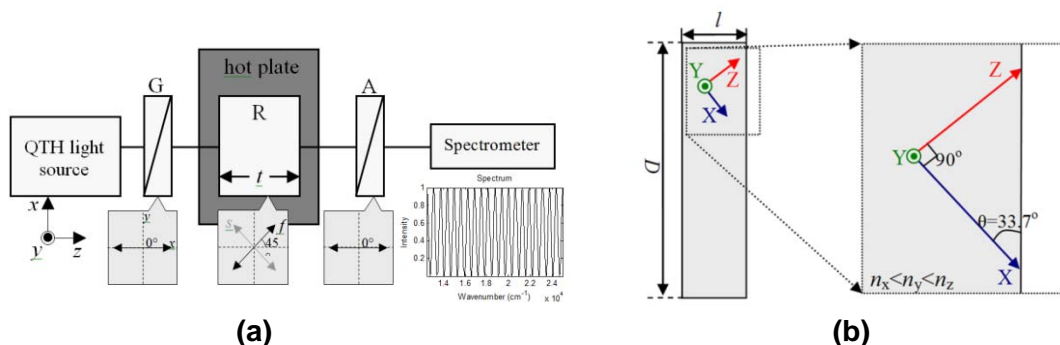


Figure 7. ACSP design and testing. (a) Experimental setup for proof of concept testing of a partial ACSP using the BTI-cut KTP retarder. (b) The BTI retarder is produced using the TI-angle identified by Ebberts [9].

For the spectral measurement, the output of the analyzer is focused into a fiber that is connected to an Ocean Optics HR2000 UV-Vis spectrometer operating over a spectral range of $\lambda = 200$ – 1100 nm with a pixel resolution of 0.44 nm. Overall, based on the optical component's spectral passbands, the system is capable of spectropolarimetric measurements over wavelengths spanning 500 to 750 nm.

When using a single high order BTI retarder, the system operates as a partial channeled spectropolarimeter. The configuration depicted in Figure 7 (a) is capable of measuring S_1 and S_3 , with intensity I given by Eq. 2 with $\phi_1 = 0$, or

$$I(\sigma) = \frac{1}{2} \left[S_0(\sigma) + S_1(\sigma) \cos(\phi_{BTI}(\sigma)) + S_3(\sigma) \sin(\phi_{BTI}(\sigma)) \right], \quad (24)$$

where $\phi_{BTI}(\sigma) = 2\pi\sigma(n_y - n_{xz})l$ is the phase difference introduced by the KTP retarder. The effective index n_{xz} is the index of refraction in the xz -plane (perpendicular to n_y), given by

$$n_{xz} = \frac{n_x n_z}{\sqrt{n_x^2 \sin^2(\theta) + n_z^2 \cos^2(\theta)}}. \quad (25)$$

In Eq. 25, θ is defined relative to the face of the retarder, as indicated in Figure 7 (b). For TI performance, $\theta = 33.7^\circ$ ($\pm 0.5^\circ$) was used when specifying the crystal axes orientation for retarder fabrication. Using $\lambda = 700$ nm, $n_{xz}(\lambda) \sim 1.785$, $n_y(\lambda) \sim 1.764$, the OPD introduced by the BTI retarder is approximately 97 μm .

The temperature of the crystal was varied via thermal conduction using the hotplate. Temperature monitoring was accomplished using two thermocouples placed along the perimeter (non-imaging side) of the crystal approximately 180° apart. Figure 8 (a) provides simulated spectra for the ACSP setup, using an estimate of the QTH source spectrum, for three different crystal temperatures ranging from ambient room temperature to 21° C above ambient. Figure 8 (b) depicts the experimentally measured modulated spectra acquired using the ACSP prototype. Note that in both cases, the frequencies of the modulations are invariant as a function of temperature and therefore exhibit the desired TI properties.

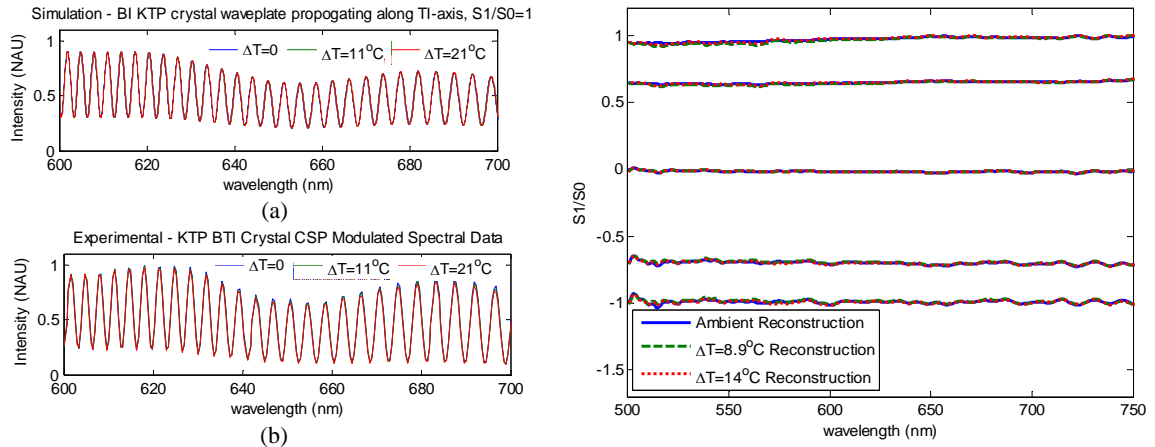


Figure 8. Simulated (a) and experimental (b) ACSP modulated spectral data for ambient, $+11^\circ\text{C}$ and $+21^\circ\text{C}$ above ambient. The consistency in the carrier frequency is indicative of the thermal stability of the retarder. Example reconstructions from the ACSP prototype are depicted in (c).

To quantify the thermally-induced errors in reconstructed spectropolarimetric data products, the generating polarizer G was used to produce different linear input polarization states ranging from horizontal (0° , $S_1/S_0 = 1$) to vertical (90° , $S_1/S_0 = -1$) in 22.5° increments. Note that while the

ACSP prototype is capable of measuring S_3 , G can only produce linear polarization states and a measurement of S_1 is sufficient for demonstrating the ACSP concept. Each state was measured with the prototype system at the ambient room temperature of 21.4 °C. Additionally, a reference polarization measurement at 157° ($S_1/S_0=0.707$) was also obtained at the ambient room temperature. Next, the retarder was heated to temperatures of 30.3 °C and 35.6 °C and two additional reference measurements were obtained. Figure 8 (c) depicts the reconstructed S_1 Stokes parameter that was produced using the three different reference measurements over the $\lambda = 500\text{-}750$ nm spectral range. Overall, the reconstructed values agree to within 1.0% RMS, and these data indicate that the spectropolarimetric reconstructions produced from this ACSP system exhibit minimal changes when the system experiences a change in temperature less than or equal to 14° C.

Finally, the experiment described above was repeated for a series of temperatures ranging from 13.3 °C to 25.7 °C above ambient. The RMS error in the reconstructed S_1 values when comparing the ambient and increased temperature reference measurements over $\lambda = 500\text{-}750$ nm are provided in Table 1. These results provide an initial quantification of the anticipated error for a given change in temperature for this KTP-based ACSP system. For comparison, a simulated partial CSP using an equivalent quartz retarder yields a reconstruction error of 183% RMS for a temperature increase from 21.4°C to 49.8°C.

Table 1. RMS error in ACSP reconstructions using ambient versus high temperature reference data.

	$\Delta T=13.3^\circ\text{C}$	$\Delta T=19.9^\circ\text{C}$	$\Delta T=25.7^\circ\text{C}$
$S_1/S_0=1.0$	1.9%	3.8%	5.2%
$S_1/S_0=0.7$	1.4%	2.9%	3.8%
$S_1/S_0=0.0$	0.2%	0.3%	0.4%
$S_1/S_0=-0.7$	1.8%	3.5%	4.6%
$S_1/S_0=-1.0$	2.6%	5.2%	6.7%

2.2 Tolerance Assessment

All the data measured with the ACSP prototype employed a collimated beam at normal incidence. To quantify the utility of the ACSP design for an imaging sensor, simulations modeling the error induced in the S_1 Stokes parameter as a function of angle of incidence (AOI) and temperature were performed for a TI-oriented KTP phase retarder. For the AOI and temperature simulations, light incident at angles ranging from $-90^\circ \leq \theta \leq +90^\circ$ and a temperature change of $\pm 30^\circ\text{C}$ were considered.

This tolerancing simulation takes into account two AOI-dependent effects. First, the refractive index, thermo-optic dispersion coefficients, and thermal expansion coefficients are a function of AOI, as expressed in Eqs. 19-21. Because the athermalization occurs at a specific propagational direction, AOI values that deviate from θ_{TI} result in thermal variability in the phase that must be accounted for. Second, the effective length of the retarder also changes as a function AOI. The results of the AOI and temperature simulation are depicted in Figure 9. This simulation was performed for a KTP-based TI retarder of a thickness that corresponds to 100 μm of OPD at $\lambda = 0.6328\mu\text{m}$. The figure illustrates that the error in the S_1 Stokes parameter vanishes at the TI-angle or when $\Delta T = 0$, as expected. The region enclosed by the white lines represents where

the error in the reconstructed Stokes parameters which will not exceed 3%. For this simulation, the normalized input S_1 value is unity.

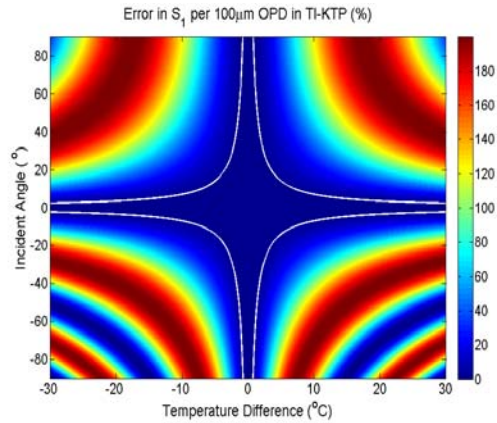


Figure 9. Error in the S_1 Stokes parameter as a function of AOI and temperature in an athermalized KTP phase retarder of $100\mu\text{m}$ OPD . The region enclosed by the white lines represents where the error will not exceed more than 3% error of the expected value at $0.6328\mu\text{m}$.

3. COMPARISON TO A MULTI-MATERIAL APPROACH

As previously mentioned, a multi-material approach for thermally stabilizing the retarders used for CSP has been suggested and demonstrated by Snik et al. [10] using MgF_2 and AlO_3 (sapphire). Using an optimized thickness ratio for each material (2.3:1 was used for MgF_2 : AlO_3), the combination of the thermo-optic constants results in a composite phase delay that is nearly independent of temperature at a given wavelength. The approach was experimentally demonstrated using 1.10 mm of AlO_3 and 2.53 mm of MgF_2 (together introducing approximately 21 μm of OPD) and the maximum residual phase error was found to be 1.5×10^{-2} rad/ $^\circ\text{C}$ over 550-750 nm. This experimentally measured value is in reasonable correspondence to the maximum phase error calculated using published values for the thermo-optic constants of these materials [14], found to be 7.2×10^{-3} rad/ $^\circ\text{C}$. As cited in [10], some of this discrepancy is likely caused by uncertainty in the thermo-optic constants over the entire passband of interest.

To provide a comparison between the multi-material athermal retarder and the BTI retarder presented in the previous sections, the residual phase change (RPC) introduced by the multi-material design is assumed to be linear with retarder thickness and temperature change. Based on the experimentally measured RPC cited in [10], a MgF_2 - AlO_3 retarder that introduces the same amount of OPD as the BTI retarder (97 μm) can be expected to introduce a maximum RPC of 1.46 rad for a temperature change of 21 $^\circ\text{C}$. Conversely, using the experimental data acquired in section 2, Figure 10 depicts the RPC for the KTP BTI approach for a temperature change of 21 $^\circ\text{C}$. The maximum RPC for the KTP BTI retarder over 550-750 nm is 0.270 rad, which is over a factor of 5 improvement in thermal stability versus the multi-material approach. For comparison, the RPCs for the BTI and multi-material approaches calculated using the tabulated thermo-optic coefficient values of KTP [12], MgF_2 , and AlO_3 [14] are also depicted in Figure 10.

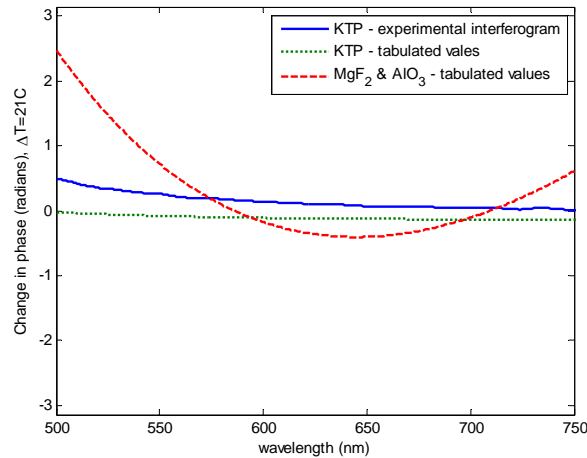


Figure 10. Comparison of RPC for the two TI retarder approaches. The experimentally measured KTP BTI RPC and the anticipated RPC, based on tabulated thermo-optic coefficients, for the KTP BTI approach are depicted along with the anticipated RPC for the multi-material approach.

While there is appreciable discrepancy between the experimentally measured and anticipated RPC values for KTP, both curves demonstrate significantly smaller RPC over the spectral passband versus the multi-material approach. While additional materials can be added to the

multi-material approach to introduce more degrees of freedom and further reduce the residual error, this process increases design complexity, cost, and size, particularly for the high order retarders needed for CSP.

This comparison of these two approaches is based on the performance of initial TI retarder designs in the visible spectral regime. In general, the RPC produced by either approach will vary depending on the materials selected. Furthermore, there are other considerations that may inform the selection of one thermal stabilization approach over the other. For example, certain systems may not be able to accommodate multiple retarder materials due to size and weight concerns, or the material needed for one approach may be unavailable or costly. The obvious design limitation for the BTI approach is the limited range of angles over which the biaxial crystal provides sufficient thermal stability, which must be considered when applying this approach in an imaging system. This is explored in section 5.

4. APPLICATION TO THE THERMAL INFRARED

The ACSP prototype in presented in section 2 demonstrated significant reduction in the thermal phase variations in a CSP. However, this set of experiments demonstrated the thermal stability of the ACSP concept only in the visible band, but there is interest in CSP-based systems in the infrared as well [5 - 6]. The two spectral regions that were explored in this work for extending the ACSP concept are the mid-wave infrared (MWIR) band of $\lambda = 3\text{-}5\mu\text{m}$ and the long-wave infrared (LWIR) thermal band of $\lambda = 8\text{-}12\mu\text{m}$. Although experiments in the infrared bands were not performed, preliminary research was pursued to determine which materials could be viable candidates for ACSP applications in these spectral regions. Orthorhombic crystals which have high transmission in the mid-wave and long-wave infrared are in general less readily available than similar crystals in the visible. Crystals with high transmission into the long-wave and the desired symmetry properties are particularly difficult to locate because they tended to still be in the research stages of development at universities and other institutions.

Examples of materials which were considered for the MWIR and their optical properties are shown in Table 2, including the birefringence at θ_{TI} when index and thermo-optic properties were available in the literature [15 - 19]. Figure 11 compares the transmission between KTP, which was used for the ACSP prototype, and RTA, a promising candidate for the MWIR athermal channeled spectropolarimeter.

Table 2. Optical properties of the MWIR candidate crystals.

Crystal Name	Transparency	n_x^1	n_y^1	n_z^1	Birefringence ^{1,2}
RbTiOPO ₄ (RTP)	0.35 - 5 μm	1.7088	1.7272	1.7657	--
RbTiOAsO ₄ (RTA)	0.4 – 5.2 μm	1.7485	1.7534	1.8090	-0.0013
CsTiOAsO ₄ (CTA)	0.35 – 5.3 μm	3.5527	3.6082	4.0236	--
KTiOPO ₄ (KTP)	0.35 – 4.5 μm	1.6726	1.6795	1.7460	0.0147
KYiOAsO ₄ (KTA)	0.53 -5.3 μm	3.3182	3.3666	3.6550	--

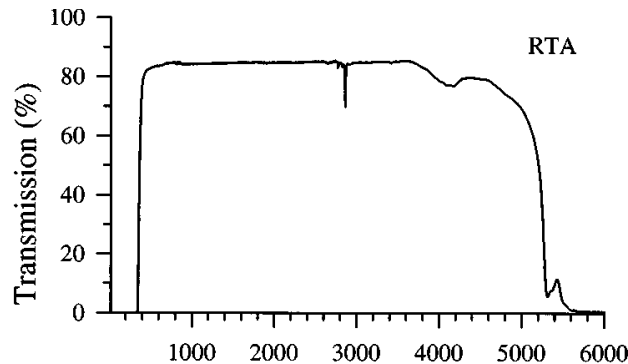


Figure 11. Transmission of RTA as a function of wavelength, in nm.

¹ Refractive index values are for $\lambda = 4\mu\text{m}$ for MWIR candidates and $\lambda = 10\mu\text{m}$ for LWIR candidates.

² Birefringence at TI-Angle

Due to the availability of thermal behavior data for RTA, this material was selected to calculate the thermally insensitive angle and to model the angle of incidence and temperature tolerances. The wavelength of $4\mu\text{m}$ was selected due to its central location in the MWIR band. The resulting TI-angle was calculated to be $\theta_{TI} = 17.09^\circ$. Figure 12 (a) illustrates the error in the S_1 Stokes parameter as a function of AOI and temperature. The region enclosed within the white lines represents deviations in temperature and angle that produce an S_1 reconstruction error of 3% or less at $4\mu\text{m}$, assuming the normalized input S_1 value is unity. The irregular shape within the white lines in Figure 12 (a) are a result of the birefringence vanishing around $\theta \sim 50^\circ$. Figure 12 (b) depicts the TI-angle as a function of wavelength. Within the $3\text{-}5\mu\text{m}$ spectral range, the TI-angle varies less than 5.8% compared to the value at $\lambda = 4\mu\text{m}$.

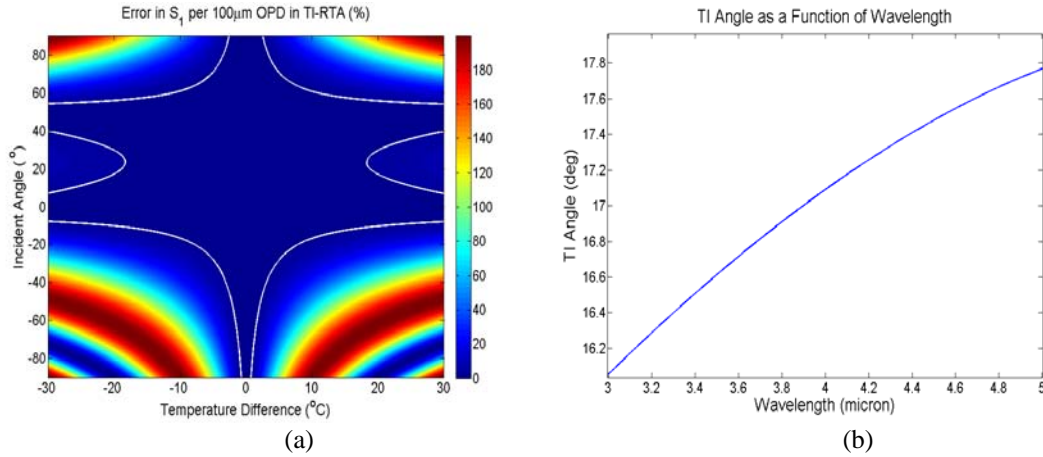


Figure 12. (a) AOI and Temperature tolerance per 100 μm OPD for an RTA TI-phase retarder. The area enclosed by the white lines represents regions which are expected to exhibit S_1 Stokes parameter reconstruction percent error of less than 3% at $\lambda = 4\mu\text{m}$. (b) TI-angle as a function of wavelength over the visible and mid-wave infrared which deviates by less than 1.04° over $3\text{-}5\mu\text{m}$ from the value at $4\mu\text{m}$.

The materials considered for the LWIR are listed in Table 3, along with some of their relevant optical properties including the birefringence at θ_{TI} when the dispersion and thermo-optic data were available [20 - 25]. Due to its relatively large spectral passband and available thermal property information, LISe was selected as a possible candidate for ACSP applications in the LWIR, and the TI-angle and tolerances of LISe were calculated. The TI-angle was calculated to be $\theta_{TI} = 35.91^\circ$ at $10\mu\text{m}$ and is depicted in Figure 14 (a) as a function of wavelength for the LWIR. The values for θ_{TI} are almost constant in the LWIR. This is due to the flattening of the thermo-optic dispersion equations. Also, the tolerances for LISe were calculated at $10\mu\text{m}$ and are depicted in Figure 14 (b) for an assumed input S_1 value of unity.

Table 3. Optical properties of LWIR candidate crystals.

Crystal Name	Transparency	n_x^1	n_y^1	n_z^1	Birefringence ^{1,2}
LiGaS ₂ (LGS) 0 0	0.8-9.1μm	3.9267	4.0943	4.0837	--
LiGaSe ₂ (LGSe) 0 0	1-9μm	4.6745	4.9230	4.9193	--
Tl ₃ PbBr ₅ 0	0.4-24μm	--	--	--	--
LiInS (LIS) 0	1-9μm	3.0420	3.1503	3.1987	-0.0645
LiInSe (LISe) 0	1-11μm	2.5089	2.5375	2.7455	0.0457
AgGaGeS (AGGS) 0	1-11μm	4.8715	5.0032	5.0032	--

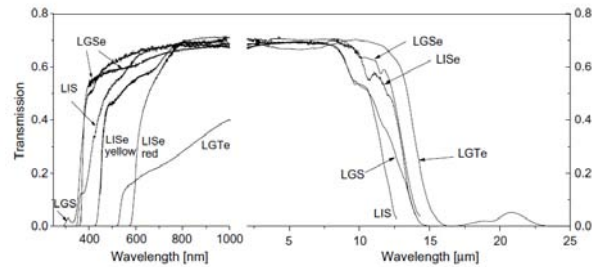


Figure 13. Transmission of LISe and other similar materials. LGTe has a larger transmission range but this material does not have an orthorhombic crystalline structure.

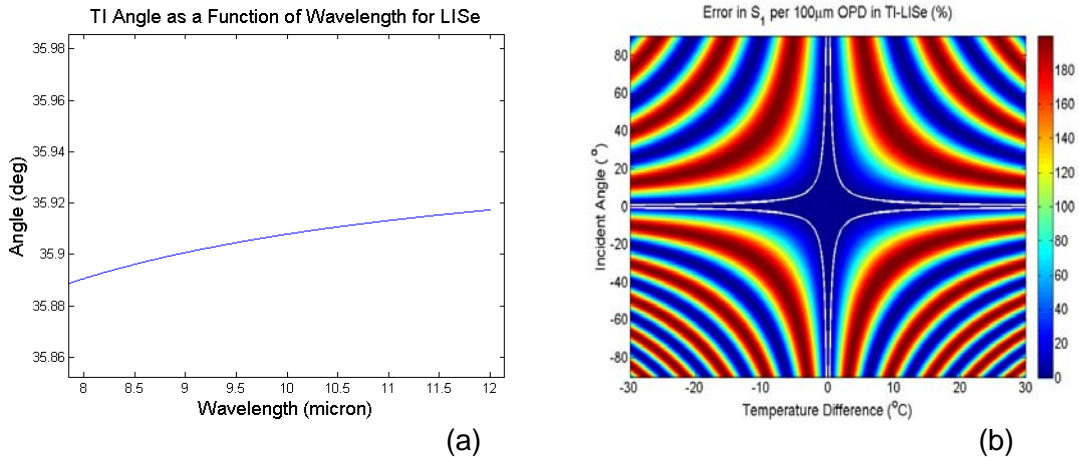


Figure 14. (a) TI-angle as a function of wavelength in LISe which deviates by less than 0.02° over 8-12 μm. (b) AOI and Temperature tolerance per 100μm OPD for a LISe TI-phase retarder. The region enclosed by the white lines represents where S₁ reconstruction will exhibit a percent error of less than 3% at 10μm.

5. SNAPSHOT IMAGING SPECTROPOLARIMETER DESIGN

Based on the results from the ACSP proof of concept experiments in the visible, a design concept for a short wavelength infrared (SWIR) snapshot imaging spectropolarimeter system was developed. The system is referred to as the snapshot compact athermal multispectral polarimetric imager (SCAMPI) and combines the athermal CSP concept with a snapshot image slicing spectrometer (ISS) to provide a complete linear spectropolarimetric measurement in a single integration time. The ISS concept was originally developed for astronomical applications [26-29] and more recently applied to high resolution microscopy in the visible [30-32]. For SCAMPI, the ISS technique has been implemented to produce a remote sensing system operating over the passband of InGaAs detectors in the SWIR ($\lambda = 0.9 - 1.7 \mu\text{m}$).

A two retarder design could be used to provide a complete polarization measurement for SCAMPI. However, for remote sensing applications, measurement of S_3 is often unnecessary as S_3 is infrequently observed in passive remote sensing [7]. Instead, measurement of S_1 and S_2 to quantify linear polarization signatures is preferable. Furthermore, measurement of S_1 and S_2 in a single CSP channel maximizes the spectral resolution of each Stokes parameter measurement and improves the SNR of the S_2 measurement by a factor of 2 versus a conventional two element CSP approach. Thus, SCAMPI implements a partial CSP design using a single TI retarder element, similar to the ACSP prototype discussed in section 2. To allow for measurement of S_1 and S_2 from a single channel, instead of S_1 and S_3 , an achromatic quarter wave retarder (such as a TIR prism) is incorporated before the TI retarder. Assuming the analyzer is an ideal polarization element with an infinite extinction ratio, the spectral intensity for the on-axis pixel is given by

$$I(\sigma) = \frac{1}{2} [S_0(\sigma) + S_1(\sigma) \cos(\phi(\sigma)) + S_2(\sigma) \sin(\phi(\sigma))]. \quad (26)$$

A Zemax layout of the SCAMPI optical design is depicted in Figure 15. The polarization analyzing elements are incorporated before the imaging optics and the ISS elements. After passing through the ACSP optics, foreoptics are used to image the scene onto a reflective image slicer, which provides an image mapping capability that will be discussed shortly. Upon reflection, the light is relayed to a dispersive prism. Finally, a lenslet array is used to image the dispersed image slices onto an FPA. The SCAMPI system operates at $f/3.6$, with a 23.6 mm effective focal length and a $\pm 2.5^\circ$ full field of view (FFOV).

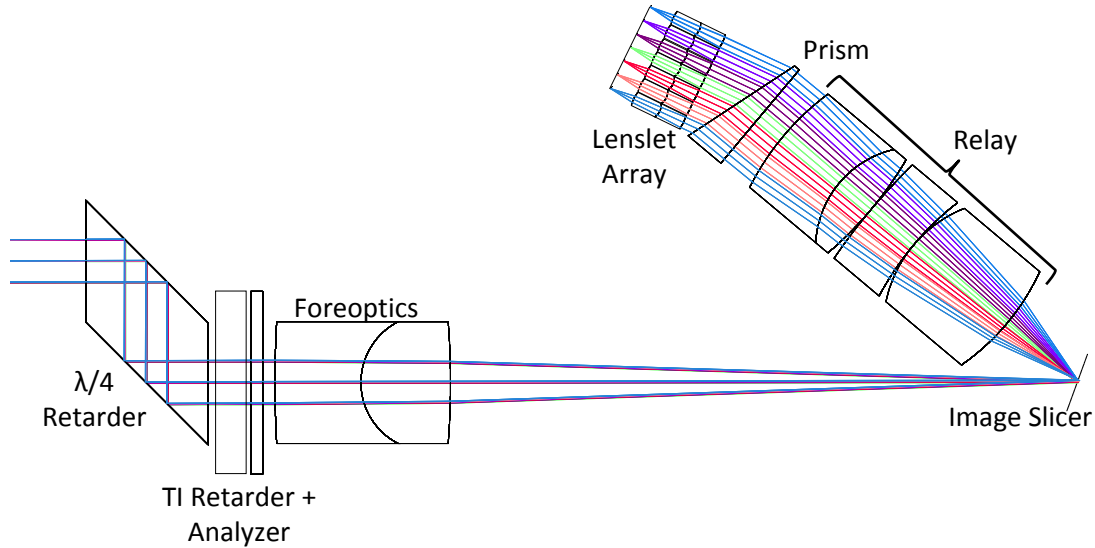


Figure 15. Zemax layout of the SCAMPI prototype. The system is designed to operate in the SWIR. Combining an ACSP with an image slicing spectrometer, the system operates as a snapshot imaging spectropolarimeter.

The image slicer component is fundamental to the snapshot operation of SCAMPI. By separating an image into a number of one dimensional spatial slices that are then dispersed by the prism element, the ISS functions as a number simultaneously operating pushbroom spectrometers that together capture a full spectral datacube. Figure 16 depicts the dispersed image slice concept. For SCAMPI, the slicer is designed to couple with a 1024 by 1280 pixel InGaAs FPA with a 15 μm pixel pitch.

In principle, an ISS has the flexibility to be designed for any combination of spatial and spectral resolutions that results in a total sampling that equals the total number of pixels on the FPA. However in practice there are some limiting factors, such as image slicer feature size and the FOV for each sub-image, which bound the achievable spatial and spectral resolutions to a much smaller design space. In the case of SCAMPI, the desired +/- 2.5 degree FFOV results in a design that produces a spatial sampling of 146 by 128 pixels over the FFOV and 70 spectral samples over $\lambda = 0.9 - 1.7 \mu\text{m}$.

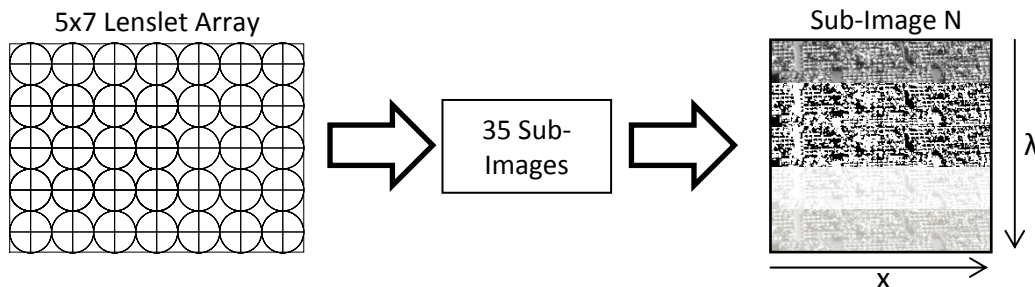


Figure 16. The SCAMPI image slicer spectrometer incorporates a 5 by 7 lenslet array that produces 35 sub-images, each containing the dispersed and CSP-modulated spectra for a one dimensional slice of the composite image.

The TI retarder for SCAMPI can be produced using either the BTI or the multi-material approach. The performance of a BTI retarder is considered first. Due to its demonstrated athermal properties and high transmission in the SWIR, KTP was selected for the BTI retarder design. While the TI angle, θ_{TI} , for KTP has been experimentally verified to be 33.7° relative to the z -axis at $\lambda = 0.633 \mu\text{m}$, to our knowledge, no experimental study has been conducted to identify θ_{TI} for KTP in the SWIR. Tabulated values for the thermo-optic properties of KTP can be used to calculate θ_{TI} using [9]

$$\theta_{TI} = \arccos \left(\frac{\left(\frac{dn_z}{dT} - \frac{dn_y}{dT} \right)^{1/2}}{\left(\frac{dn_z}{dT} - \frac{dn_x}{dT} \right)} \right). \quad (27)$$

From Eq. 27, $\theta_{TI} = 32.6^\circ$ is found for $\lambda = 1.3 \mu\text{m}$. While TI angle calculations based on tabulated thermo-optic properties are too inaccurate to provide an estimate of the TI angle without experimental validation, this value for θ_{TI} is used for this initial design, keeping in mind an experimental validation should be performed before the BTI design for SCAMPI is finalized. Based on the spectral resolution of SCAMPI, a TI retarder element that introduces $\sim 28 \mu\text{m}$ of OPD ensures sufficient fringe sampling across the spectral passband. For KTP and using $\theta_{TI} = 32.6^\circ$, a 1.65 mm thick retarder introduces $\sim 27.7 \mu\text{m}$ of OPD was modeled.

The thermal stability of the ACSP design was simulated over the $\pm 2.5^\circ$ FFOV of the SCAMPI sensor. For this initial design, the thermal stability was investigated for field angles in the the xz -plane (see Figure 7 (b)) of the crystal exclusively. Thus light incident on the crystal in these simulations experiences indices n_y and $n_{xz}(\theta)$, where $n_{xz}(\theta)$ is defined by Eq. 25. Due to the relatively small FFOV of the SCAMPI sensor, the index variation in the xz -plane is anticipated to be the dominant variable affecting the thermal stability of the system.

Figure 17 (a) depicts the simulated RPC for the KTP BTI design for temperature changes up to $\pm 25^\circ\text{C}$. The maximum RPC under these conditions is $\Delta\phi = 5.8 \times 10^{-2}$ rad at $\lambda = 1.3 \mu\text{m}$, or 2.3×10^{-3} rad/ $^\circ\text{C}$. The simulated maximum RPC over the operational passband of the sensor is depicted in Figure 17 (b) for the nominal value of θ_{TI} . Assuming that the fabrication tolerance on the axes orientations for the BTI element can be specified at $\pm 0.5^\circ$ (as was the case for the visible prototype), Figure 17 (b) also depicts maximum RPC for deviations of θ_{TI} value from the nominal value by $\pm 0.5^\circ$. Thus the overall maximum RPC for this BTI design is anticipated to be less than 5.2×10^{-3} rad/ $^\circ\text{C}$.

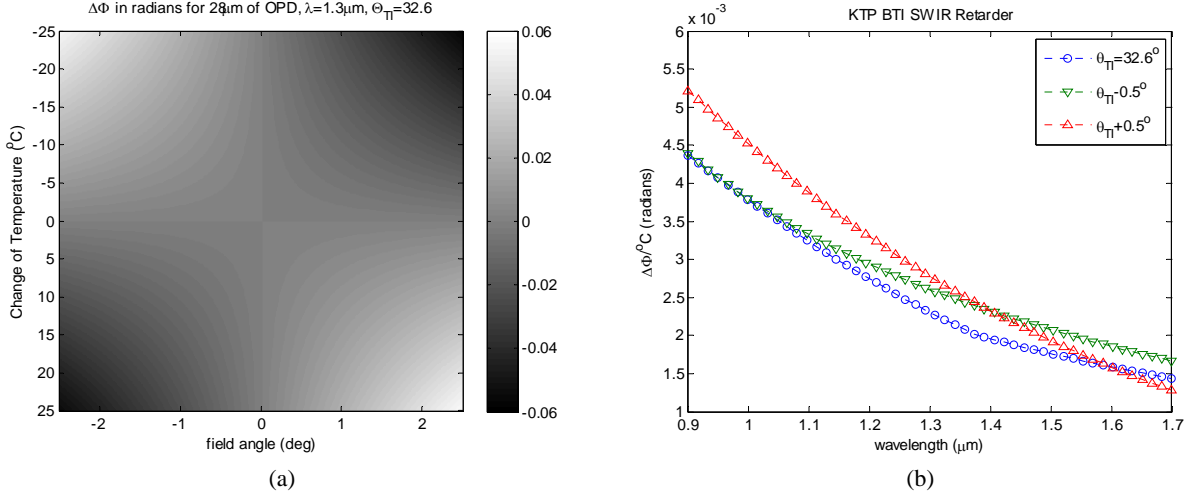


Figure 17. Residual phase change (RPC) for the KTP BTI retarder design for SCAMPI. The RPC as a function of field angle and change of temperature is depicted in (a) for $\lambda=1.3 \mu\text{m}$. The maximum RPC as a function of wavelength over the sensor passband is depicted in (b).

A multi-material approach using MgF_2 and AlO_3 was also investigated for producing a TI retarder for SCAMPI. The thickness ratio of the original visible spectrum design was modified to minimize the total phase error over the SCAMPI passband. For a 1:5.5 thickness ratio, a 0.50 mm thick AlO_3 retarder combined with a 2.75 mm MgF_2 retarder together introduce $27.9 \mu\text{m}$ of OPD. The maximum RCP over $\lambda = 0.9 - 1.7 \mu\text{m}$ for this multi-material design is $\Delta\phi = 0.21 \text{ rad}/^\circ\text{C}$, which is two orders of magnitude larger than the anticipated residual phase error for the KTP BTI approach. Thus, the thermal stabilizing properties of these materials that have been demonstrated in the visible do not extend to the SWIR. Although other materials may provide improved thermal stabilization in the SWIR over MgF_2 and AlO_3 , for the initial design of SCAMPI, the BTI approach was pursued for producing the ACSP.

Using the reconstruction equations for the reference beam calibration technique [8], the variations in the normalized Stokes parameter reconstructions caused by thermal variability are given by

$$\hat{S}_{1,out} = \hat{S}_{1,in} \cos(\Delta\phi) - \hat{S}_{2,in} \sin(\Delta\phi), \text{ and} \quad (28)$$

$$\hat{S}_{2,out} = \hat{S}_{1,in} \sin(\Delta\phi) + \hat{S}_{2,in} \cos(\Delta\phi). \quad (29)$$

In Eqs. 28 and 29, the $\hat{\cdot}$ denotes normalized Stokes parameters, the subscript ‘out’ indicates the reconstructed values, the subscript ‘in’ indicates the true Stokes parameter values, and $\Delta\phi$ denotes the RPC of the BTI retarder. Because S_1 and S_2 are measured in a single channel, the reconstruction errors for these Stokes parameters are coupled. Thus the maximum reconstruction error in S_1 for a change in retarder phase of $\Delta\phi$ is dependent on the amplitude of S_1 as well as the amplitude of S_2 . For example, maximum reconstruction error in S_1 at $\lambda = 1.3 \mu\text{m}$ for the SCAMPI design occurs for $S_1 = 0.0303S_0$ and $S_2 = 0.9995S_0$, while the minimum error in S_1 occurs for $S_1 = S_0$ and $S_2 = 0$. The deviations in the reconstructed Stokes values ($|\hat{S}_{1,out} - \hat{S}_{1,in}|$) are simulated in Figure 18 for these two cases and are linear with temperature variation. For the case

simulated in Figure 18 (a), the deviation in the reconstructed normalized S_1 value at the 2.5° field angle is $2.65 \times 10^{-3}/^\circ\text{C}$ and is $8.77 \times 10^{-5}/^\circ\text{C}$ for the case simulated in Figure 18(b). While in some circumstances the edges of the FFOV are subject to large deviations in Stokes parameter reconstructions for large temperature changes, the majority of the SCAMPI field of view enjoys low reconstruction errors for substantial temperature changes.

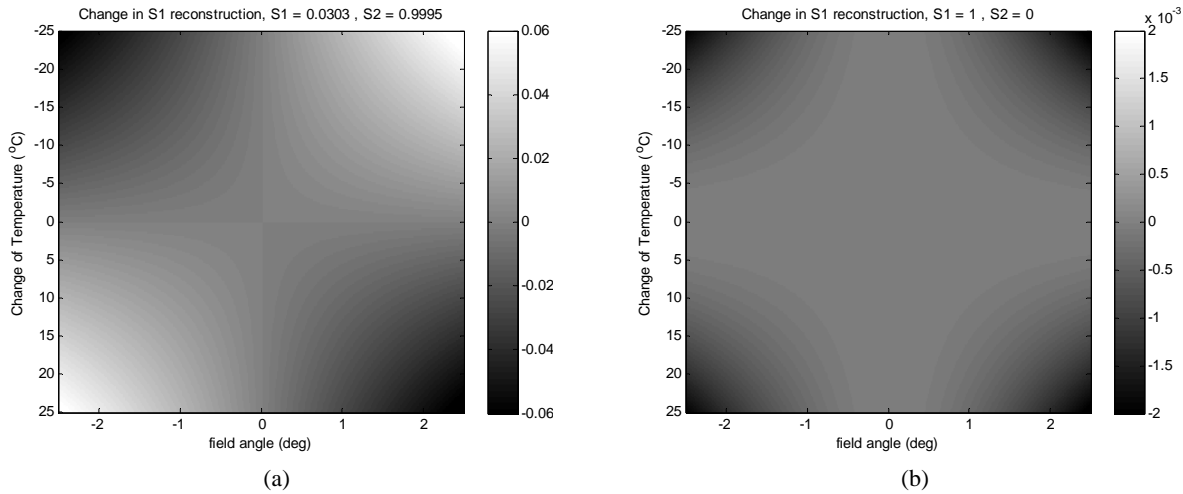


Figure 18. Deviations in the reconstructed Stokes parameters for the Stokes parameter values producing (a) the maximum reconstruction error and (b) the minimum reconstruction error.

Using the spectral resolution of the SCAMPI system, Figure 19(a) and (b) simulate the fringe profile for the on-axis and $(2.5^\circ, 0^\circ)$ field points, respectively. The fringe profiles are depicted for temperature changes up to 25°C and demonstrate the anticipated thermal stability of the retarder’s carrier frequency over this temperature range.

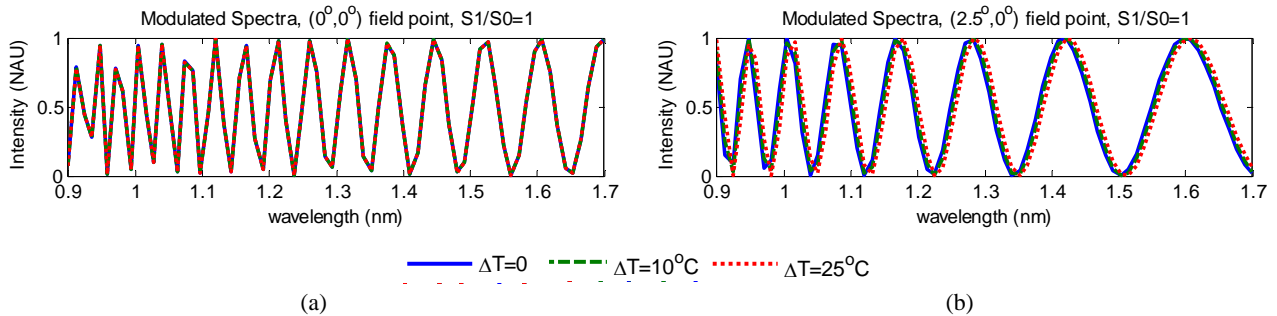


Figure 19. Fringe profiles for (a) the on-axis field point and (b) the $(2.5^\circ, 0^\circ)$ field point for the SCAMPI design using a KTP BTI retarder.

6. CONCLUSIONS

This paper presents a technique that provides enhanced thermal stability for CSP retarders versus the previous state of the art. While the design work presented in this paper is focused on athermalizing a channeled spectropolarimeter system specifically for remote sensing applications, nearly every application of channeled spectropolarimetry can benefit from a reduced need to recalibrate or update calibration data. The BTI technique utilizes readily available and inexpensive KTP to provide an athermalized CSP solution through the SWIR. However, it is worth noting that there are other materials, such as RTA and LISe that possess the biaxial orthorhombic crystal properties that could potentially expand the implementation of this ACSP technique to the MWIR and LWIR.

Based on the results of initial proof of concept studies, a system that can provide snapshot imaging spectropolarimetric measurements in the SWIR was developed. The snapshot compact athermal multispectral polarimetric imager (SCAMPI) uses the thermally stable BTI retarder concept combined with an image slicing spectrometer to produce a snapshot spectropolarimetric measurement over a 5 degree FFOV and $\lambda = 0.9\text{-}1.7 \mu\text{m}$ using 146 by 128 spatial samples and 70 spectral samples.

7. REFERENCES

1. K.H. Nordsieck, "A simple polarimetric system for the Lick Observatory Image-Tube Scanner," *Pub. Astron. Soc. Pac.*, 86(511), 324 – 329 (1974).
2. K. Oka, and T. Kato, "Spectroscopic polarimetry with a channeled spectrum," *Opt. Lett.*, 24, 1475-1477 (1999).
3. D. Sabatke, A. Locke, E.L. Dereniak, M. Descour, and J. Garcia. "Snapshot imaging spectropolarimeter," *Opt. Eng.* 41(5), 1048-1054 (2002).
4. S.H. Jones, F.J. Iannarilli, and P.L. Kebabian, "Realization of quantitative-grade fieldable snapshot imaging spectropolarimeter," *Opt. Exp.*, 12(26), 6559 – 6573 (2004).
5. M. W. Kudenov, N. A. Hagen, E. L. Dereniak, and G. R. Gerhart, "Fourier transform channeled spectropolarimetry in the MWIR," *Opt. Exp.*, 15, 12792–12805 (2007).
6. J. Craven-Jones, M.W. Kudenov, M.G. Stapelbroek, and E.L. Dereniak, "Infrared hyperspectral imaging polarimeter using birefringent prisms," *Appl. Opt.*, 50(8), 1170-1185 (2011).
7. J.S. Tyo, D.L. Goldstein, D.B. Chenault, and J.A. Shaw, "Review of passive imaging polarimetry for remote sensing applications," *Appl. Opt.*, 45(22), 5453 – 5469 (2006).
8. A. Taniguchi, K. Oka, H. Okabe, and M. Hayakawa, "Stabilization of a channeled spectropolarimeter by self-calibration," *Opt. Lett.*, 31, 3279-3281 (2006).
9. C. Ebberts, "Thermally insensitive, single-crystal, biaxial electro-optic modulators," *J. Opt. Soc. Am. B*, 12(6), 1012-1020 (1995).
10. F. Snik, T. Karalidi, and C.U. Keller, "Spectral modulation for full linear polarimetry," *Appl. Opt.*, 48(7), 1337-1346 (2009).
11. J.D. Bierlein and H. Vanherzeele, "Potassium titanyl phosphate: properties and new applications," *J. Opt. Soc. Am. B*, 6(4), 622-633 (1989).
12. W. Wiechmann, S. Kubota, T. Fukui, and H. Masuda, "Refractive-index temperature derivatives of potassium titanyl phosphate," *Opt. Lett.*, 18(15), 1208-1210 (1993).
13. J. Craven-Jones, B.M. Way, M.K. Kudenov, and J.A. Mercier, "Athermalized channeled spectropolarimetry using a biaxial potassium titanyl phosphate crystal," *Opt. Lett.*, 38(10), 1657-1659 (2013).
14. G. Ghosh, *Handbook of Thermo-Optic Coefficients of Optical Materials with Applications*, Academic Press (1988).
15. C.S. Tu, R. S.Katlyar, V. H. Schmidt, R. Guo, A.S. Bhalla, "Hypersonic anomalies and optical properties of RbTiOAsO₄ and KTiOPO₄ single crystals," *Phy. Rev. B* 59, 251-256 (1999).
16. G.M. Loiacono, D.N. Loiacono, R.A. Stolzenberger, "Crystal growth and characterization of ferroelectric CsTiOAsO₄," *Journal of Crystal Growth*, 131, 323 -330 (1993).
17. L.T. Cheng, L.K. Cheng, J.D. Bierlein, F.C. Zumsteg, "Nonlinear optical and electrooptical properties of single crystal CsTiOAsO₄," *Appl. Phys. Letter*, 63, 2618-2620 (1993).
18. sales@newlightphotonics.com (personal communication, November 21, 2012)
19. D.L. Fenimore, K.L. Schlepler, "Infrared correct Sellmeier coefficients for potassium titanyl arsenate," *J. Opt. Soc. Am. B*, 12, 794-796 (1995).
20. L. Isaenko, A. Yeliseyev, S. Lobanov, A. Titov, V. Petrov, J.-J. Zondy, P. Krinitsin, A. Merkulov, V. Vedenyapin, J. Smirnova, "Growth and properties of LiGaX₂ (X = S, Se, Te) single crystals for nonlinear optical applications in the mid-IR," *Cryst. Res. Technol.*, 38, 379 -387 (2003).

21. V. Petrov, A. Yelisseyev, L. Isaenko, S. Lobanov, A. Titov, J.-J. Zondy, "Second harmonic generation and optical parametric amplification in the mid-IR with orthorhombic biaxial crystals LiGaS₂ and LiGaSe₂", *Appl. Phys. B*, 8, 543-546 (2004).
22. M. Velázquez, A. Ferrier, J.-L. Doualan, R. Moncorgé (2012). *Rare-Earth-Doped Low Phonon Energy Halide Crystals for Mid-Infrared Laser Sources*, Solid State Laser, Prof. Amin Al-Khursan (Ed.), ISBN: 978-953-51-0086-7, In Tech, Available from: <http://intechopen.com/books/solid-state-laser/rare-earth-doped-phonon-energy-halide-crystals-for-mid-infrared-laser-sources>
23. L. Isaenko, A. Yelisseyev, S. Lobanov, P. Krinitsin, V. Petrov, J.-J. Zondy, "Ternary chalcogenides LiBC₂ (B=In, Ga; C = S, Se, Te) for mid-IR nonlinear optics", *J. Non. Crystl. Solids*, 352, 2440 – 2443 (2006).
24. K. Miyata, V. Petrov, K. Kato, "Phase matching properties for AgGaGeS₄", *Applied Optics*, 46, 5728 – 5731 (2007).
25. A.P. Yelisseyev, V.A. Drebuschak, A.S. Titov, L.I. Isaenko, S. I. Lobanov, "Thermal properties of midinfrared nonlinear crystal LiInSe₂", *J. App. Phy.*, 96, 3659-3665 (2004).
26. L. Weitzel, A. Krabbe, H. Kroker, N. Thatte, L. E. Tacconi-Garman, M. Cameron, and R. Genzel, L. E. Tacconi Garman, M. Cameron and R. Genzel, "3D: The next generation near-infrared imaging spectrometer," *Astron. Astrophys. Suppl. Ser.*, 119(3), 531–546 (1996).
27. S. Vivès, and E. Prieto, "Original image slicer designed for integral field spectroscopy with the near-infrared spectrograph for the James Webb Space Telescope," *Opt. Eng.*, 45(9), 093001 (2006).
28. F. Henault, R. Bacon, R. Content, B. Lantz, F. Laurent, J. Lemonnier, and S. Morris, "Slicing the universe at affordable cost: the quest for the MUSE image slicer," *Proc. SPIE*, 5249, 134–145 (2004).
29. J. A. Smith, "Basic principles of integral field spectroscopy," *N. Astron. Rev.*, 50(4-5), 244–251 (2006).
30. L. Gao, R.T. Kester, and T.S. Tkaczyk, "Compact image slicing spectrometer (ISS) for hyperspectral fluorescence microscopy," *Opt. Exp.*, 17(5), 12293-12308 (2009).
31. L. Gao, R.T. Kester, N. Hagen and T.S. Tkaczyk, "Snapshot Image Mapping Spectrometer (IMS) with high sampling density for hyperspectral microscopy," *Opt. Exp.*, 18(14), 14330-14344 (2010).
32. N Bedard, N. Hagen, L. Gao, and T.S. Tkaczyk, "Image mapping spectrometry: calibration and characterization," *Opt. Eng.*, 51(11), 111711 (2012).

DISTRIBUTION

1	MS0899	Technical Library	9536 (electronic copy)
1	MS0359	D. Chavez, LDRD Office	1911



Sandia National Laboratories